

A novel X-ray diffractometer for studies of liquid–liquid interfaces

Bridget M. Murphy,^{a,b*} Matthais Greve,^a Benjamin Runge,^a Christian T. Koops,^a Annika Elsen,^a Jochim Stettner,^a Oliver H. Seeck^c and Olaf M. Magnussen^{a,b}

^aInstitute for Experimental and Applied Physics, University of Kiel, D-24098 Kiel, Germany,

^bRuprecht Haensel Laboratory, University of Kiel, D-24098 Kiel, Germany, and ^cDeutsches Elektronen-Synchrotron DESY, Notkestrasse 85, D-22603 Hamburg, Germany.

*E-mail: murphy@physik.uni-kiel.de

The study of liquid–liquid interfaces with X-ray scattering methods requires special instrumental considerations. A dedicated liquid surface diffractometer employing a tilting double-crystal monochromator in Bragg geometry has been designed. This diffractometer allows reflectivity and grazing-incidence scattering measurements of an immobile mechanically completely decoupled liquid sample, providing high mechanical stability. The available energy range is from 6.4 to 29.4 keV, covering many important absorption edges. The instrument provides access in momentum space out to 2.54 \AA^{-1} in the surface normal and out to 14.8 \AA^{-1} in the in-plane direction at 29.4 keV. Owing to its modular design the diffractometer is also suitable for heavy apparatus such as vacuum chambers. The instrument performance is described and examples of X-ray reflectivity studies performed under *in situ* electrochemical control and on biochemical model systems are given.

Keywords: liquid–liquid interfaces; gas–liquid interfaces; X-ray scattering in structure determination; X-ray diffractometer.

© 2014 International Union of Crystallography

1. Introduction

The study of liquid interfaces is of vital importance for understanding many fundamental phenomena in physics, chemistry and biology as well as in applied problems in material processing, biomedical research, marine and environmental science (Fukuto *et al.*, 1999). Topics of particular interest include liquid metal and alloy interfaces, phospholipid–protein interactions, mineralization at liquid interfaces, model membrane interfaces, electrochemical interfaces, and the rapidly increasing field of nanoparticle growth processes. However, an in-depth understanding of these interfaces is still hampered by the lack of detailed data on the nanoscale structure and dynamics of these systems. Surface X-ray scattering methods belong to the very few experimental approaches that provide such data, even for interfaces between two extended immiscible liquid phases, *in situ* with atomic scale resolution. For the free surfaces of liquids in contact with a gas phase, extensive studies of the vertical and in-plane structure have been performed by X-ray reflectivity, diffuse X-ray scattering, and grazing-incidence X-ray diffraction, providing a wealth of quantitative results on the surface structure of dielectric (Braslau *et al.*, 1988; Ocko *et al.*, 1994) and metallic liquids (Barton *et al.*, 1986; Bosio *et al.*, 1984; Dimasi *et al.*, 1998; Magnussen *et al.*, 1995), surface segregation (Regan *et al.*, 1997; Shpyrko *et al.*, 2006), surface phase transitions

(Deutsch *et al.*, 1995; Wu *et al.*, 1993), and the structure and phase behaviour of organic layers on liquids (Kraack *et al.*, 2002; Magnussen *et al.*, 1996; Weinbach *et al.*, 1994). In contrast, investigations of the deeply buried interfaces between two liquids are scarce and have been performed only for a few selected systems (see, for some examples, Bosio *et al.*, 1984; Duval *et al.*, 2012; Gründer *et al.*, 2011; Luo *et al.*, 2006; Tamam *et al.*, 2011; Schlossman & Tikhonov, 2008). This is mainly due to the much greater experimental difficulties in accessing these interfaces. A good overview of such studies may be found in the book by Pershan & Schlossman (2012).

A key technique in the study of fluid interfaces is X-ray reflectivity, which can access the molecular-scale interface structure even in the absence of long-range order. In these experiments one measures, as a function of incident angle α , the fraction of the specularly reflected X-ray intensity I at the reflection angle $\beta = \alpha$. Owing to the rapid decay of $I(\alpha)$ with increasing α , the reflected X-ray intensity has to be measured over many orders of magnitude, requiring at large α the subtraction of background contributions such as the scattering of the liquid bulk sample (usually collected by moving the detector out of the plane of reflection). The reflectivity $R = I(\alpha)/I_0$ is directly determined by the total electron density profile across the interface region. For most liquid interfaces R is well described by Pershan's Master equation (Pershan & Als-Nielsen, 1984), which states that R is the Fresnel reflectivity

tivity R_F of a perfectly sharp interface, multiplied by the square of the Fourier transform of the gradient $d\langle\rho_{el}(z)\rangle/dz$, where $\langle\rho_{el}(z)\rangle$ is the electron density averaged within the surface plane.

Laboratory reflectometers offer comparatively low intensities and hence are limited to reflectivity measurements over maximal eight orders of magnitude, which reduces the range of surface normal momentum transfer q_z and consequently the spatial resolution. For this reason, most current studies of liquid interfaces employ synchrotron radiation sources which permit reflectivity measurements into the 10^{-9} to 10^{-10} range. In particular, studies of liquid–liquid interfaces, where I is severely reduced by absorption losses in the bulk liquid, are only feasible at insertion device beamlines of third-generation synchrotron facilities.

As liquids cannot be tilted, the experimental geometry requires special considerations. This geometry may be easily realised on a laboratory source by moving the anode (Weiss *et al.*, 1986), but such investigations are possibly limited due to a lack of intensity. Modern third-generation synchrotron radiation sources can provide orders of magnitude higher intensity and so are very attractive for studying weakly scattering systems such as liquids. However, the experimental geometry is more complicated since it is necessary to deflect the beam down using X-ray optics. Similar designs (*e.g.* Als-Nielsen, 1984; Lin *et al.*, 2003; Pershan *et al.*, 1987; Pershan & Als-Nielsen, 1984; Schlossman *et al.*, 1997; Smilgies *et al.*, 2005; Yano *et al.*, 2009) achieve this by using a set-up similar to a triple-axis neutron spectrometer. In this arrangement the beam moves on the surface of a cone with the tip at the deflecting optics and therefore both the sample and the detector have to be moved vertically and horizontally to follow the beam, as illustrated schematically in Fig. 1(a). These movements, which are required for each new angle of incidence α on a reflectivity curve, can involve up to six motors and inevitably mechanically excited vibrations on fluid sample surfaces. Even when using state-of-the-art active vibration isolation units, a waiting time of 2–30 s, depending upon the sample system, is required to allow the vibrations at the liquid sample surface to decay before data collection can continue, limiting the possibilities for kinetic experiments. Obviously, it is preferable for any measurement of a fluidic interface to avoid any possible source of external excitation, *i.e.* minimize mechanical motions of the sample. More recently a high-energy design employing Laue diffraction was developed for investigating buried liquid interfaces (71 keV) (Honkimäki *et al.*, 2006). The Liquid Interface Scattering Apparatus (LISA) presented in this paper operates with two crystals scattering in Bragg geometry. Following a similar concept to that of LISA (Murphy *et al.*, 2010), a specialized instrument designed under space constraints had been devised at Diamond Light Source and optimized for studies at liquid–vapour interfaces operating in an energy range from 12.5 keV to 30 keV (Arnold *et al.*, 2012). The LISA diffractometer has unique features as compared with both the ESRF and Diamond instruments, which will be discussed in this work. LISA is a dedicated liquid spectrometer installed at beamline P08 of the PETRA III

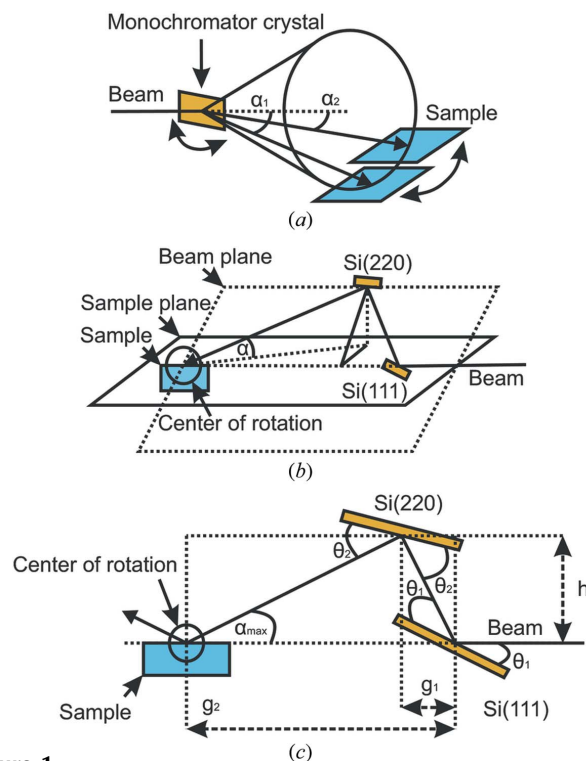


Figure 1 (a) Single deflecting crystal liquid scattering geometry. (b) Double-crystal Bragg deflecting geometry including (c) important angles and distances.

third-generation synchrotron source at DESY delivering an intense beam over the complete q -range at photon energies from 6 to 30 keV, enabling studies of deeply buried liquid–liquid interfaces and additionally acts as a heavy duty diffractometer. Here we provide a detailed description of this instrument, detailing its concept, technical implementation, design parameters and specific advantages. Furthermore, characteristic examples of the data obtainable with the LISA diffractometer are briefly discussed.

2. Principle of operation

LISA operates by means of an asymmetric tilting double-crystal monochromator in Bragg geometry (called the beam-tilter in the following) as illustrated schematically in Fig. 1(b). The horizontal incoming X-ray beam is scattered upwards *via* Bragg reflection at a first crystal and then bent downward again using a second crystal with a larger Bragg angle, defining a plane as at the liquid scattering apparatus at Diamond (Arnold *et al.*, 2012). The sample is placed at the intersection of this beam plane with a horizontal plane defined by the incoming beam at angle of incidence $\alpha = 0$ ('sample plane'). The sample is positioned so that the studied interface is in the sample plane, and the centre of the sample, which coincides with the axis of the detector rotation, is located at the intersection of the original incoming beam [dashed line in Fig. 1(b)] and the twice-deflected beam. By rotating the crystals around the incoming beam axis the angle of incidence α can be varied from 0 to a maximum angle α_{max} , defined by the difference in the scattering angles of crystal 1 (θ_1) and crystal 2 (θ_2),

$$\alpha_{\max} = 2(\theta_2 - \theta_1). \quad (1)$$

From Bragg's law, $\theta = \arcsin[\lambda/(2d)]$, where d is the lattice parameter and λ the wavelength, and the relation of energy and wavelength ($\lambda = hc/E$, where h is Planck's constant and c is the speed of light), we have the energy-dependent maximum angle,

$$\alpha_{\max}(E) = 2[\arcsin(hc/2d_{220}E) - \arcsin(hc/2d_{111}E)]. \quad (2)$$

The X-ray beam is also moving on the surface of a cone but, in contrast to the single-crystal liquid diffractometer, now the cone tip is on the sample surface. When the energy is changed the height of the second crystal has to be corrected so that the cone tip stays within the centre of the sample surface. At first glance, Fig. 1(c) suggests that the incidence point of the X-ray beam on the second crystal could have the distance g_1 , which would give a very simple relation for the height of the second crystal: $h_1 = g_1 \tan(2\theta_1)$. Unfortunately then the distance to the sample g_2 would vary with energy. In order to keep a constant beam position on the sample for different energies, g_1 has to be fixed. As a result it is necessary to vary the height of the second crystal leading to the relation

$$h(E) = g_1 \tan[2\theta_1(E) - \theta_2(E)] + g_2 \tan[\alpha_{\max}(E)] \frac{\tan[2\theta_1(E)] - \tan[2\theta_1 - \theta_2(E)]}{\tan[2\theta_1(E)] + \tan[\alpha_{\max}(E)]}. \quad (3)$$

Since the intersection of the (twice-reflected) incident beam with the sample plane is independent of the rotation angle, α can be varied without changes in the sample position by rotating the double-crystal monochromator (mchi) around the beam axis where the maximum angle of incidence α_{\max} is described by

$$\alpha(\text{mchi}) = \arcsin[\cos(\text{mchi}) \sin(\alpha_{\max})]. \quad (4)$$

However, this rotation also causes a change in the direction of the reflected beam, making it necessary to move the detector to follow the scattered beam. The angle of the detector (dth) is described by

$$\text{dth}(\text{mchi}) = \arctan[\sin(\text{mchi}) \tan(\alpha_{\max})]. \quad (5)$$

In this set-up, movements of the sample are only required to shift the position of the beam on the sample or to rotate the sample, which is only necessary for samples with directional in-plane order. Reflectivity and surface scattering studies of liquid surfaces and interfaces can be fully performed without any sample motion. Furthermore, the sample stage can be completely mechanically decoupled from the beam-tilter and the detector unit, thus eliminating motor-induced vibration at the sample. This ensures maximal sample stability and eliminates the need for waiting times after motor movements, making rapid data collection possible.

The aim to maximize the reflected signal of the X-rays for liquid–liquid interfaces requires that one must carefully choose the energy to minimize adsorption while maximizing the scattering cross section by selecting a high enough energy. Recent studies have shown that, particularly for investigations

of biological systems, energies in the range 24–34 keV are desirable to optimize the diffraction intensity while minimizing radiation damage (Nave & Garman, 2005; Paithankar & Garman, 2010). In this region the energy is sufficiently high to minimize photoelectric absorption while being low enough to optimize the interaction cross section relative to the degree of damage due to Compton scattering which can result in bond breaking and secondary beam damage due to free radicals (Honkimaäki *et al.*, 2006). As investigations of liquid–liquid interfaces usually require transmission through some 50 mm bulk liquid, on the one hand sufficiently high energies of ≥ 20 keV are required for typical liquids such as aqueous solutions or organic solvents. On the other hand, the brilliance of typical third-generation synchrotron sources usually steeply decays in that energy range, requiring optimization of the employed energy for the system under study. Typically, the optimum energy window lies between 20 and 35 keV. This window is also particularly well suited for the study of organic matter, *i.e.* some of the most interesting liquid–liquid systems. This energy range is too low for high-energy optics in Laue geometry as the absorption at the reflection crystals would be too high.

Furthermore, this energy range includes the *K*- or *L*-edges of many interesting elements, allowing element-specific enhancement of the scattering contrast *via* anomalous scattering techniques. For example, it may be interesting to investigate samples with elements relevant for biological and material science applications such as the heavy elements, palladium and silver at liquid–liquid interfaces. At the liquid–vapour interface, where lower photon energies may be used, other interesting species such as iron or copper are also accessible.

3. Experimental set-up

The P08 high-resolution diffraction beamline (Seeck *et al.*, 2012), situated on a high- β section at the PETRA III third-generation synchrotron radiation source, provides a highly monochromatic low-divergent X-ray beam. The beam, delivered by a 2 m-long undulator (Barthelmess *et al.*, 2008), is first monochromated by a liquid-nitrogen-cooled double-crystal monochromator (FMB Oxford) consisting of two Si(111) crystals. Following this, the beam is diverted vertically by 1250 mm *via* a large-offset monochromator equipped with two pairs of crystals. The Si(311) combination provides photon energies between 5.4 and 18.4 keV with an energy resolution $\Delta E/E = 3 \times 10^{-5}$ to 6×10^{-5} and the Si(511) pair provides energies between 8.4 and 29.4 keV with $\Delta E/E = 2 \times 10^{-5}$ to 4×10^{-5} over the given energy range. The large-offset monochromator also provides suppression of higher harmonics by a factor of 10^8 . The inclusion of Be compound refractive lenses currently operating in a slightly focusing mode for LISA provides a flux of 2×10^{11} counts s^{-1} and a beam size of 40 μm vertically and 800 μm horizontal at the LISA sample position. The beam divergence is 20 $\mu\text{rad} \times 9 \mu\text{rad}$ FWHM (horizontal *versus* vertical) (Barthelmess *et al.*, 2008); the energy resolution is as listed above.

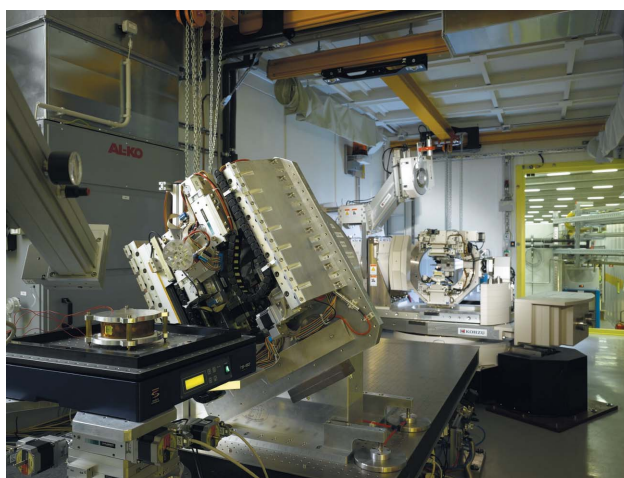
The LISA instrument is positioned towards the rear of the P08 hutch (Fig. 2*a*). The individual elements of the diffractometer (deflecting optic, sample stage and detector stage) are decoupled from each other to increase the stability of each module and to prevent unwanted vibrations from reaching the liquid sample during experiments. The beam-tilting device shown in Fig. 3(*a*) is mounted on an optical table (Instrument Design Technology, Widnes, UK) equipped with encoder-controlled stepper motors for pitch, yaw and roll (range $\pm 1^\circ$, accuracy $1 \mu\text{rad}$) and vertical and horizontal alignment (range $\pm 20 \text{ mm}$, accuracy $1 \mu\text{m}$). These movements are used to align the tilting optic centre of rotation at the beam position and parallel to it. Movement of the beam-tilter along the beam direction for the initial coarse positioning is enabled *via* air pads under the housing.

The beam is tilted by an asymmetric double-crystal set-up mounted in the beam-tilter, consisting of a Si(111) and Si(220) crystal to bend the incoming X-ray beam down onto the sample (Murphy *et al.*, 2010). The crystals may be rotated

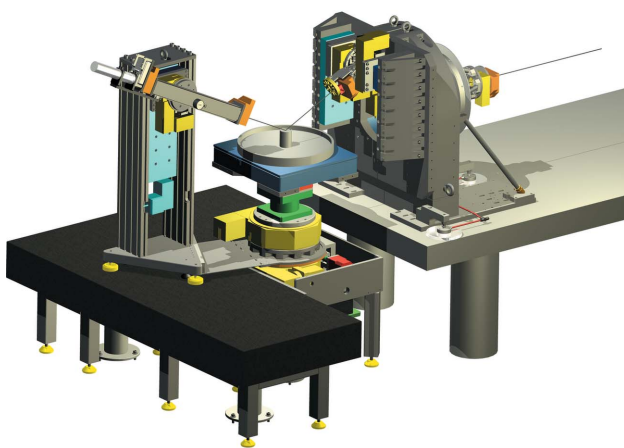
Table 1
Momentum range and resolution for various X-ray energies.

Energy (keV)	$q_{z(\text{max})}$ (\AA^{-1})	Δq_z (\AA^{-1})	$q_{x(\text{max})}$ (\AA^{-1})	Δq_x (\AA^{-1})
6.40	2.70	5.89×10^{-5}	3.23	1.13×10^{-5}
8.00	2.64	7.66×10^{-5}	4.03	1.41×10^{-5}
12.00	2.58	1.19×10^{-4}	6.05	2.12×10^{-5}
18.00	2.56	1.80×10^{-4}	9.07	3.18×10^{-5}
25.00	2.55	2.52×10^{-4}	12.6	4.41×10^{-5}
29.40	2.54	2.96×10^{-4}	14.8	5.19×10^{-5}

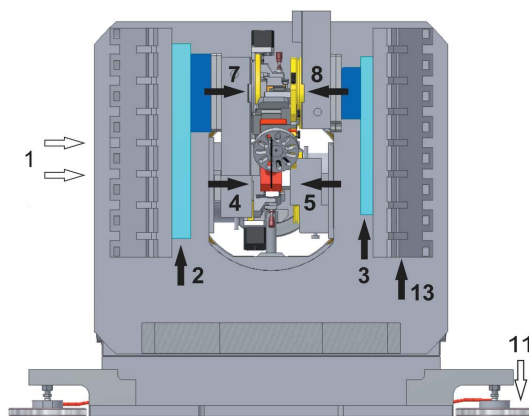
about the X-ray beam axis in order to change the angle of incidence (see Figs. 2 and 4). Grazing-incident scattering measurements are easily performed by rotating the detector arm horizontally (both clockwise and anticlockwise rotation is possible). With the current choice of Si crystals it is possible to reach a q_z maximum (Fig. 4*c*) of at least 2.54 \AA^{-1} over the entire energy range as shown in Table 1. The resolution is determined by the angular divergence.



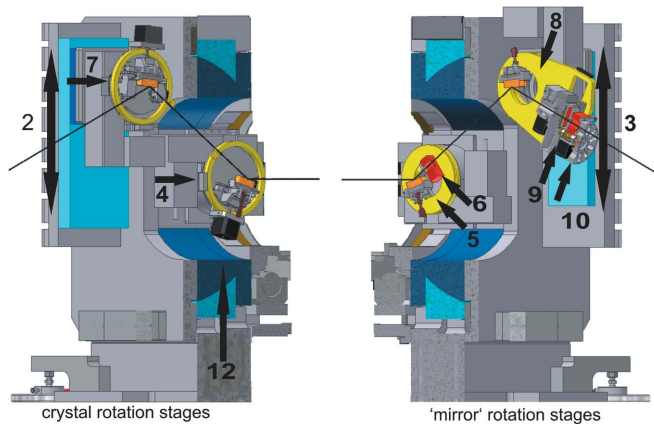
(*a*)



(*b*)



(*a*)



(*b*)

(*c*)

Figure 3
The LISA diffractometer beam-tilting component. Schematic views of (*a*) the front view of the beam-tilter and ‘explosion drawing’ with the beam-tilter opened along the centre axis. Shown are (*b*) the crystal translation and rotation stages and (*c*) the ‘mirror’ translation and rotation stages. The Bragg crystals are shown on both sides to illustrate the geometry. The central components are: (1) tilt stage housing, (2) translation for second crystal, (3) ‘mirror’ translations, (4) first crystal rotation, (5) first crystal ‘mirror’ rotation, (6) ion chamber, (7) second crystal rotation, (8) second crystal ‘mirror’ rotation, (9) diamond diode and ion chamber, (10) absorber wheel, (11) air pads for stage positioning, (12) rotating air bearing for the tilter, (13) tilter reinforcement.

Figure 2
(*a*) LISA as installed at PETRA III beamline P08 (foreground, left to right: detector arm and slits, sample stage and beam-tilter; background: the P08 high-resolution diffractometer). Photograph courtesy of DESY. (*b*) The LISA diffractometer consisting of three modules. From right to left: detector stage, sample stage and double-crystal beam-tilter.

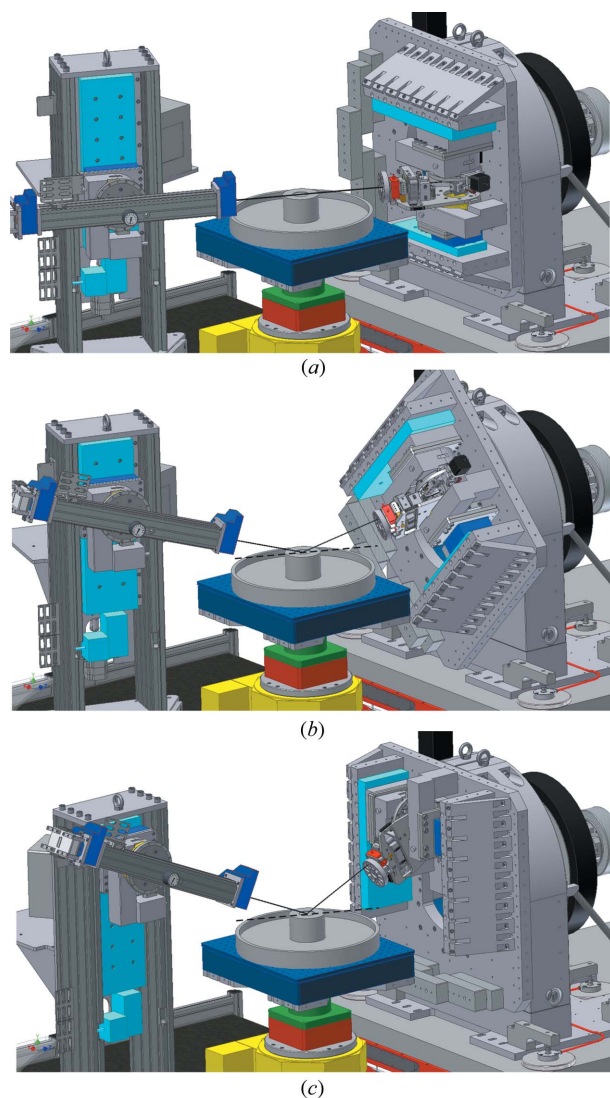


Figure 4
Illustration of the beam-tilter rotation during reflectivity measurements. The position of the beam-tilter rotation (mchi) is shown at (a) $mchi = 0$, $\alpha = \beta = 0^\circ$, (b) $mchi$ at 45° , $\alpha = \beta = 4.1^\circ$ and (c) at 90° , $\alpha = \beta = 5.8^\circ$ at the maximum position of the angles α and β . The detector height, vertical and horizontal translation and rotations follow the reflected beam.

Grazing-incident scattering measurements are easily performed by rotating the detector arm horizontally. In the horizontal scattering direction the maximum q_x range is significantly larger and depends on the energy chosen (see Table 1); for both q_z and q_x the resolution is limited by the beam divergence. Both crystals of the beam-tilter are mounted on a single rotation (named mchi) so that motor movements are minimized during measurements. The rotation stage (ESS, Germany) operates with air bearings and has a remarkable 60 nm sphere of confusion and a wobble of 0.9 μrad . It is implemented with a rotation with minimum step size of 5×10^{-8} rad so that the instrumental resolution is a factor of ten better than the divergence-limited resolution. In the current implementation the stage can be rotated by 270° so that it is possible to impinge upon the liquid interface from above or below by rotating the beam-tilter around its axis. Owing to the high precision of the air bearing, rotation of the

angle of incidence and thus instrumental momentum resolution in q_z of 0.003 \AA^{-1} in full step encoder operation is available; in practice by micro-step operation this value is improved by a factor of 1000. This means that the resolution is not instrumentally limited and the beam divergence is the critical factor. The rotation stage is mounted in a custom-designed housing constructed to conserve the accuracy of the rotation stage. This construction provides excellent stability and a high degree of accuracy for maintaining the crystal position in the incoming X-ray beam.

The two deflecting crystals have two rotational degrees of freedom (Bragg angle rotation and a 1° yaw movement) to centre the crystal surface on the rotation axis and a translation (5 mm) to align them at the centre of rotation of the device. The first crystal rotation is on the right-hand side of the beam-tilter as shown in Fig. 3(c). A second low-resolution rotation stage, carrying an ion chamber for diagnostic purposes, is positioned at the left-hand side. This so-called ‘mirror stage’ keeps the device balanced during rotation. To facilitate energy change, the second crystal sits on a 200 mm translation stage with encoder feedback [Figs. 3(b) and 3(c)]. With a similar symmetry consideration a mirrored construction consisting of a rotation stage on a long linear translation and mounted across from the second crystal carries the monitoring ion chamber, beam-position-sensitive diamond diode, absorber wheel and the sample slits [Figs. 3(b) and 3(c)]. Additional supports are mounted on both sides of the housing to increase the stiffness. Using this symmetric construction all elements are well balanced and so unwanted beam movements at the sample due to changing forces are reduced to $\pm 1 \mu\text{m}$ during rotation over 90° . The beam can be monitored *via* ion chambers after each crystal with an additional position-sensitive transmitting diamond quadrant diode after the second crystal. This allows each crystal to be independently aligned. Both the second ion chamber and the diamond quadrant detector can be used as a monitor for the incident beam intensity. The beam impinging on the sample is defined by a rotating slit system, centred on the beam axis, mounted on the beam-tilter rotation stage after the Si(220). The rotation keeps the slit vertically oriented, *i.e.* parallel to the sample surface during the beam-tilter rotation by rotating the slits in the opposite direction. It provides a significant reduction in background and additionally allows the optimization of the beam footprint at the sample for low angles. The final element before the sample is an absorber wheel consisting of varying thicknesses of aluminium. The operating energy of the beam-tilter is changed by selecting the Bragg angles for both crystals and translating the second crystal perpendicular to the rotation axis (Fig. 5) as well as performing the associated movement with the ‘mirror’ stages.

The sample stage, as shown in Fig. 6(a), is an independent structure consisting of a granite block on a kinetic mount and can support sample cells weighing up to 150 kg. Directly above the granite block a thick-walled aluminium cylinder extends through the detector rotation circle without touching it, on which sits the sample rotation stage. For sample alignment two horizontal translation stages and a vertical translation are

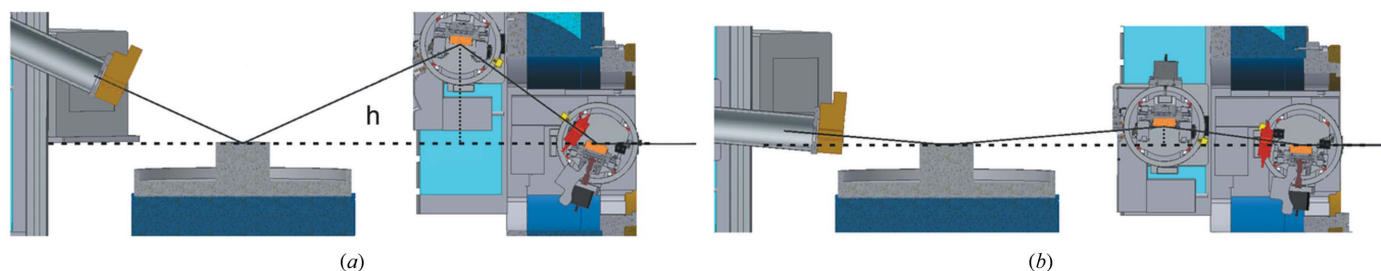


Figure 5 Height and angles for detector arm (left) and tilting crystal (right) are shown for (a) 29.4 keV and (b) 6.4 keV. To select an energy both crystals are rotated to the required Bragg angle and the second crystal is translated to the appropriate height h . The detector angle and height are chosen accordingly. The black line shows the X-ray beam path; the horizon is shown with a dashed line. The Si crystals mounted on the beam-tilter are shown in orange.

provided. An active anti-vibration stage is mounted on top for further reduction of mechanical noise. In the in-beam direction the maximum sample size is 400 mm. In the horizontal direction space is not limited.

The detector stage is mounted on a large L-shaped polished granite slab allowing the detector to run on air pads (Fig. 6*b*). The detector rotation is mounted on the granite block, sitting around the aluminium cylinder of the sample stage and connected to the detector arm *via* a metal plate, allowing high-resolution rotation of the detector arm on the air pads without mechanical coupling to the sample. Its rotation axis can be centred on the sample rotation axis *via* two translations. The detector arm consists of a translation and rotation in the vertical plane. The sample-to-detector distance may be varied between 0.5 m and 1.3 m. The momentum range in q_x extends from 0 to 4 \AA^{-1} with a resolution of 0.03 \AA^{-1} or better (the full range is shown in Table 1). For reflectivity measurements the beam-tilter is rotated around its central axis to change the incident angle, and the corresponding exit angle is chosen by

changing the horizontal and vertical rotation as well as the height of the detector arm. This means that the sample remains stationary during reflectivity scans and the detector moves to follow the specular reflection or any chosen offset of the specular scan direction; therefore, the system is not disturbed during measurements and a significant reduction in data collection time results, as will be illustrated later.

The LISA spectrometer is controlled by *SPEC* (Swislow, 1996); all critical axes are fitted with an encoder. A combination of five- and two-phase stepper motors is controlled *via* a VME control system. The individual hardware components are compatible with DESY standards. Access to the beamline control system is *via* a TANGO interface (Chaize *et al.*, 1999). This allows elements such as the beam energy, the optical table and a fast shutter to be incorporated into the LISA control system.

While a selection of detectors is available, the current standard is a Mythen strip detector (Dectris), with a $50 \mu\text{m}$ pixel size, which can be mounted vertically or horizontally depending on the application. A Roper Scientific two-dimensional detector is also available upon request. A high-speed high-resolution two-dimensional Eiger detector (DECTRIS) was also made available in 2013.

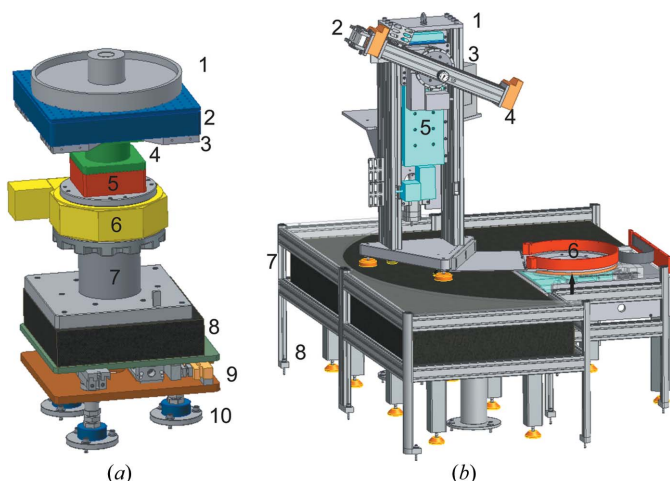


Figure 6 (a) Schematic view of the sample stage: (1) sample, (2) antivibration table, (3) table mounting plate, (4) height translation stage, (5) horizontal translation stages, (6) sample rotation stage, (7) support column designed to pass through the detector rotation stage, (8) granite base plate, (9) translational adjustment, (10) three height-adjustable feet. (b) Schematic view of the detector stage: (1) detector stand mounted on air pads, (2) one-dimensional detector arm and rotation, (3) two-dimensional detector support, (4) detector slit, (5) height translation, (6) rotation stage, (7) granite plate, (8) support feet and guard rail.

4. Diffractometer alignment

For the operation of the beam-tilting optics it is crucial that the axis of the main rotation $mchi$ and the pivot points of both deflecting crystals are aligned precisely along the incoming synchrotron beam. For stable operation an angular stability of less than half the FWHM of the Darwin width of the beam-tilter crystals during $mchi$ rotation is required [Darwin width of Si(220) at 25 keV = $7.3 \mu\text{rad}$ FWHM (Stepanov, 2013)]. Angular instabilities can cause changes in the angle of incidence, decreases in the Bragg-reflected intensity and, in the extreme case, result in the loss of the Bragg condition. In order to allow for the diffractometer alignment each crystal has two rotational degrees of freedom (Bragg angle rotation and perpendicular tilt) and a translation to centre the crystal surface on the rotation axis.

The first step in the alignment procedure is to position the crystals in the centre of the incoming X-ray beam and correct the angular misalignment using the yaw and pitch movements on the optical table. Initially, this is made by adjusting the

crystal surfaces parallel to the beam and blocking half of the transmitted beam intensity. The alignment of the table's translations and rotations is iteratively refined until the intensity is constant over a rotation of $m\chi$ by 180° (Fig. 7a), indicating that the beam-tilter is aligned almost concentric to the X-ray beam. As this method is not accurate enough to obtain the top performance of the beam-tilter, a similar procedure is repeated using the Bragg reflection of the first crystal. To confirm the angular alignment of the beam-tilter to the incoming beam, rocking scans of the first crystal at beam-tilter positions of 0° , 90° and 180° are required. Once again the angular and translational motors of the optical table are used to position the axis of the beam-tilter. As shown in Fig. 7(b), Bragg-peaks positions show little deviation between the beam-tilter axis and the beam once the instrument is aligned. To complete the fine alignment of the beam-tilter the procedure is repeated with the second crystal. The presence of in-beam detectors such as the ion chambers after each crystal facilitates a speedy alignment. The alignment and tracking is checked by monitoring the intensity at the detector while scanning over the full $\alpha = -\beta$ range. At this point the beam

tilter is concentric to the incoming X-ray beam. However, it is now necessary to define 0° rotation of the incident angle α and the corresponding $m\chi$ value at the horizon. For this purpose a large water trough is mounted and aligned in the beam. The zero position for the beam-tilter rotation with respect to the horizon is determined by scanning the incoming and outgoing angles $\alpha = \beta$ symmetrically typically $\pm 0.1^\circ$ about the 'zero' point. Any offset in the centre of this scan is due to a tilt in the incoming synchrotron beam and may be corrected by setting the new zero. At this point LISA is aligned.

5. Performance

In order to execute a reflectivity scan, the beam-tilter rotates azimuthally around the synchrotron beam axis and so scattering varies from horizontal at the low angles of incidence to vertical at the highest angles as shown earlier in Fig. 4. Due to the changing scattering geometry, the intensity varies because of polarization effects. At energies above 20 keV the intensity loss due to polarization is less than 10% over a full beam-tilter rotation. At lower energies polarization effects reduce the intensity at low angles of incidence but, as in reflectivity this is the high-intensity regime, this is not critical. Other losses of photon flux do not appear: owing to the low divergence of PETRA III and the pre-LISA energy selection earlier in the beamline by the Si(311) or Si(511) in the P08 non-dispersive large-offset monochromator (Seeck *et al.*, 2012), LISA provides close to 80% transmission after correcting for polarization effects at 9 keV and 90% at 25 keV (Fig. 8) for the collimation P08 configuration. This is in stark contrast to Arnold *et al.* (2012) who state that the throughput is just 10% for $q_z = 0$ and 50% for q_{max} at their instrument. The difference in transmitted intensity at both instruments is due to two contributions. For example, considering $q_z = 0$, first a factor of three to four of the loss at I07 (Arnold *et al.*, 2012) is due to the higher horizontal divergence at Diamond as compared with PETRA III (this is a real intensity win at LISA), and addi-

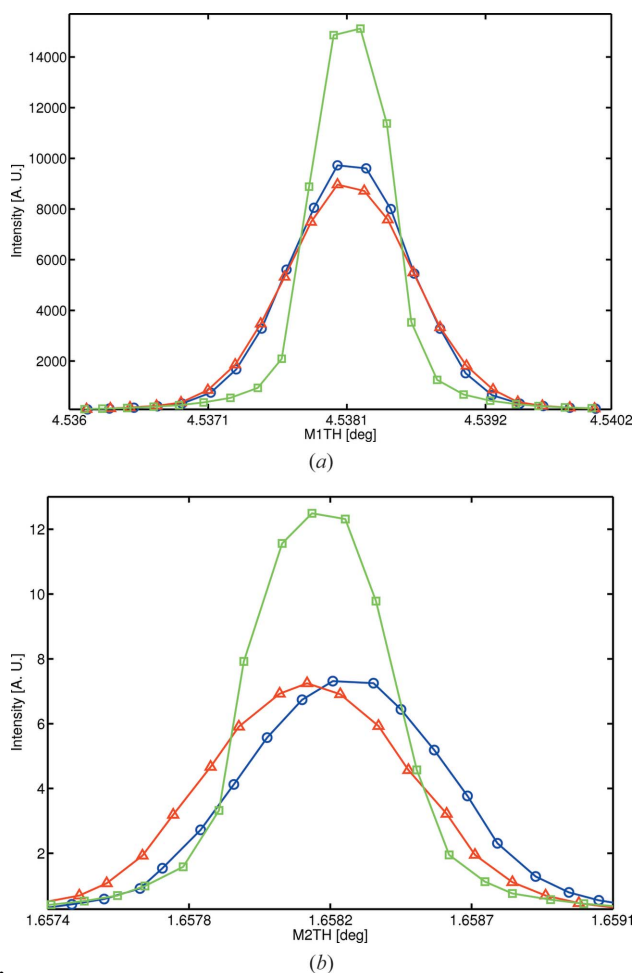


Figure 7 Rocking curve of (a) the first crystal and (b) the second crystal of the beam-tilter at $m\chi = 0, 90$ and 180° . The convergence of the Bragg peaks shows that the incidence angle of the beam on both crystals is stable with rotation of the beam-tilter rotation indicating high angular stability of the beam-tilter. Red triangles: 0° ; green squares: 90° ; blue circles: 180° .

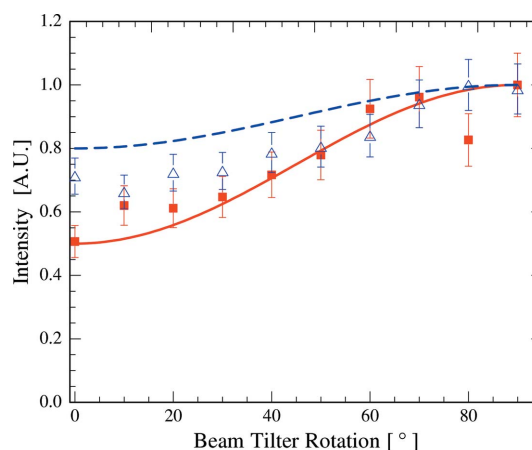


Figure 8 Intensity measured at the sample position during a 90° rotation of the beam-tilter at 9 keV (red closed squares) and at 25 keV (blue triangles). Symbols represent the collected data; the continuous line is the calculated polarization dependence at 9 keV (red) and at 25 keV (blue, upper line). The corresponding α_{max} for 9 keV is 16.69° and for 25 keV is 5.78° .

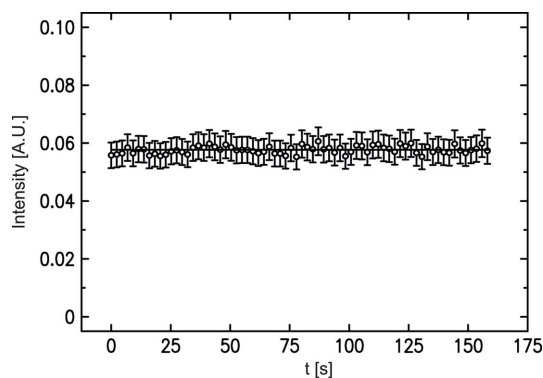


Figure 9
Time scan of reflected intensity from a water sample at $q_z = 0.1 \text{ \AA}^{-1}$ after change of the incidence angle at $t = 0 \text{ s}$. No intensity change due to vibrations could be monitored. $E = 25 \text{ keV}$.

tionally a factor of two to three of the loss is observed at I07 due to the use of a lower index Si(111) in the beamline optics as compared with Si(311) or Si(511) in the P08 large-offset monochromator (this is intensity that is lost at P08 before the X-rays reach LISA). It is possible to scan the energy at LISA for applications such as anomalous scattering. This is a complicated procedure as it requires a synchronous movement of all monochromators on the beamline. First tests have shown that a step size of 1 eV or less is achievable over a range of $\pm 100 \text{ eV}$. Ultimately an energy resolution of between 0.02 eV at 6 keV and 0.4 eV at 30 keV is attainable as determined by the Darwin width of the Si(111) first LISA tilt crystal.

In a series of tests the angle of incidence was changed and the time response of the reflected intensity was observed. These tests confirmed that there is no loss of intensity (due to possible vibrations) induced by the move (Fig. 9). This is in stark contrast to the case on a traditional liquid reflectometer where up to 30 s waiting time is required to reach the maximum intensity. As there is no requirement to move the sample for isotropic liquids, this greatly reduces waiting times which currently slow data collection at conventional liquid surface diffractometers.

6. Sample environments

For liquid samples one generally chooses a surface as large as possible to minimize curvature effects due to the meniscus and therefore maximize the flat cross section for scattering. For liquid–liquid interfaces one must consider many factors. Minimizing absorption means minimizing the X-ray path through the liquid so that a small sample cell may be beneficial.

On the one hand the same problems with sample curvature as for liquid–vapour interfaces exist, requiring sufficiently large samples with an adequate flat surface area for reflectivity measurements.

Especially for samples with high surface tension such as mercury or certain oils, the liquid meniscus can extend over centimetres, making cell diameters of comparable size necessary. On the other hand it is important to minimize the absorption of the beam by the bulk liquid which means

keeping the X-ray path through the liquid short. The latter favours small sample cell diameters.

6.1. Liquid cells

Two types of cells have been designed for use at LISA. For studies of liquid Hg–aqueous electrolyte interfaces, X-ray electrochemical cells consisting of a 40–60 mm Kel-F trough with 0.12 mm-thick glass windows were designed housed in an outer cell equipped with Kapton windows [see Figs. 10(a)–10(c)]. Using a potentiostat (Compactstat, Ivium Technologies) and a Pt wire counter electrode the potential is controlled *versus* a Hg/Hg₂SO₄ electrode (Schott), connected to the cell *via* a liquid bridge. For X-ray reflectivity investigations on lipid monolayers at oil–water interfaces, Kel-F and teflon troughs with diameters in the range 40–50 mm have been developed [Fig. 10(d)]. These reservoir cells also have glass windows. The diameters of these cells are chosen to optimize the parameters discussed above for energies between 20 and 30 keV. Pinning the meniscus is always tricky and one has to carefully match the liquid and the cell material to achieve a positive or negative meniscus as required and obtain the flattest surface possible. We find that Teflon and Kel-F, with an inner rim to help form the meniscus, cleaned in Caro’s acid give good results. Other groups prefer to use glass cells

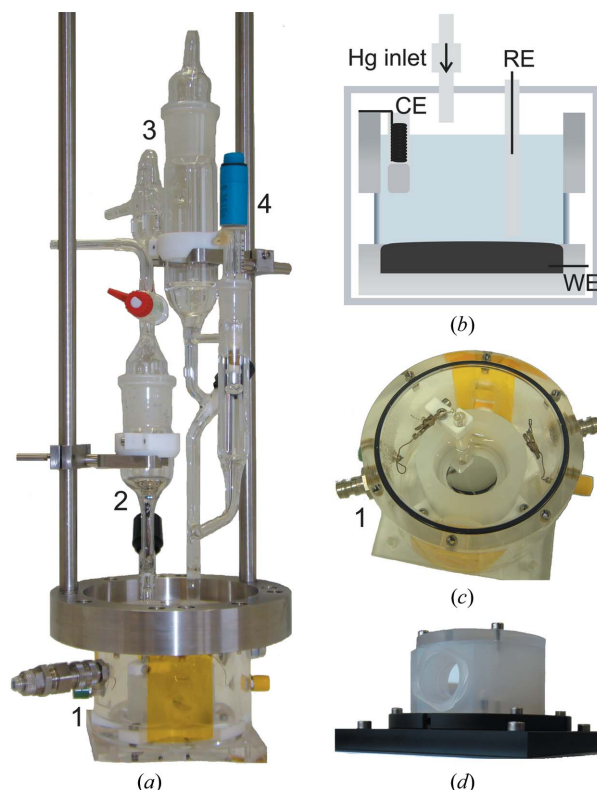


Figure 10
(a) Liquid mercury electrochemical cell shown along with (b) a schematic of the cell, where RE is the reference electrode, CE is the counter electrode and WE is the working electrode. (c) Top view of the mercury cell housing and inner chamber. The numbered items shown are (1) mercury chamber with X-ray-transmitting Kapton and glass windows and gas inlet, (2) mercury reservoir, (3) electrolyte reservoir, (4) reference electrode. (d) Lipid cell.

for similar measurements (Laanait *et al.*, 2012; Luo *et al.*, 2006).

6.2. Studies employing heavy sample environments

Due to the fact that LISA can carry heavy-duty equipment up to 150 kg and offers enough space for a large chamber, it is possible to use the instrument as a heavy-duty scattering diffractometer as illustrated in the next example. A dedicated UHV chamber with a variable magnetic field for *in situ* growth and magnetic measurements has been developed and is currently in use at the LISA instrument. The chamber shown in Fig. 11 is optimized for reflectivity and grazing-incidence scattering. The sample has two positions in the chamber. In the growth position a sputter gun and evaporators are available for preparing and growing thin layers. The sample is then translated to the measurement position within a beryllium dome without breaking vacuum. As the sample is mounted on an annealing stage, it can be heated in both positions to change the growth parameters or for *in situ* investigations of temperature-related effects. A variable magnetic field up to 47 mT may be applied by varying the separation of permanent magnets.

The UHV chamber is currently employed for *in situ* studies of metal oxide interfaces, in particular of magnetoelectric interfaces between piezoelectric and magnetostrictive compounds (Abes *et al.*, 2013). Typically a two-dimensional Roper detector is used for grazing-incidence scattering data collection. Possible future applications of this or similar sample environments in the field of liquid interfaces are studies of liquid metals with low vapour pressure, such as liquid gallium or some ionic liquids.

7. Selected studies

7.1. Reflectivity from free water surface

As a first simple test of the instrument's capabilities, X-ray reflectivity curves of a free water surface were recorded

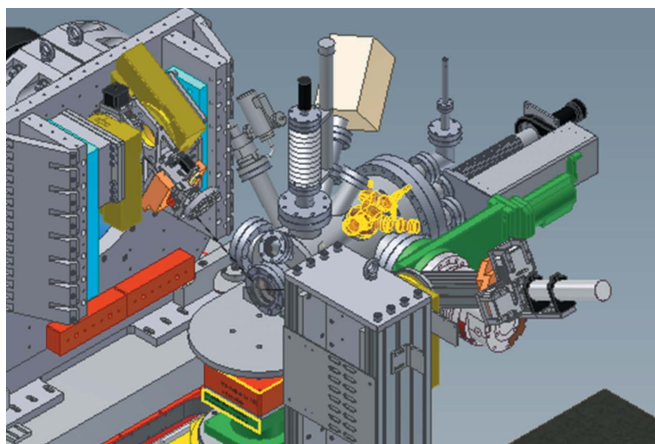


Figure 11
UHV growth chamber mounted on LISA (shown without beryllium window). The sample stage allows rotation around the surface normal for measuring grazing-incidence reflections.

employing a 20 cm-long trough of water. An example of a measured reflectivity curve (at $T = 296$ K) is shown in Fig. 12. The data are well described by a Gaussian roughness due to capillary waves of $\sigma_{\text{r.m.s.}} = 3.18 \pm 0.03$ Å, which is slightly higher than the 3 Å expected for the resolution (0.4 mrad), in good agreement with the results of Braslau *et al.* (1985) and Daillant *et al.* (1989). Carefully optimized measurements by Schwartz *et al.* (1990) and Shpyrko *et al.* (2004), aiming for an extremely high purity of the water sample and employing an inert gas atmosphere environment, obtained lower values. For the measurements here, which were taken as the last step of the instrument alignment, 18.2 M water without further purification was studied in air. In view of this, a value similar to those in the older literature (Braslau *et al.*, 1985; Daillant *et al.*, 1989) is expected. For a full discussion on this topic

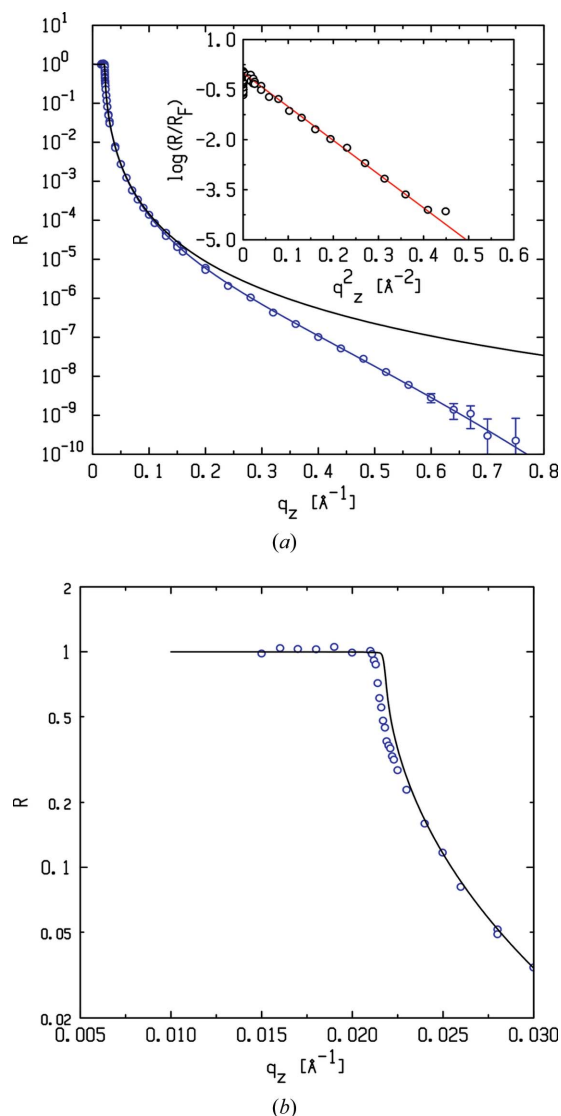


Figure 12
(a) Water reflectivity collected at 25 keV within 60 min (circles). The continuous black line shows the ideal Fresnel reflectivity for water and the blue line shows the Fresnel reflectivity with a roughness of 3.18 ± 0.03 Å. The inset shows $\log(R/R_F)$ over q_z^2 . (b) Reflectivity close to the critical angle.

see Pershan & Schlossman (2012). The main aim of the measurement here is to illustrate that the reflectivity can be measured up to $q_z = 0.75 \text{ \AA}^{-1}$ and over ten orders of magnitude at 25 keV, illustrating the low background at LISA. The implementation of the rotating sample slit enables background reduction and high-quality data around the critical angle (Fig. 12*b*).

7.2. Adsorption at the liquid mercury–electrolyte interface

A model electrochemical system for over a century now, the liquid Hg–electrolyte interface has played a key role in the development of the electrical double layer and electrochemical adsorption (Buess-Herman, 1986; Chapman, 1913; Barnes & Gentle, 2005; Gouy, 1910; Helmholtz, 1879). Though long inaccessible *via* X-ray probes, recent developments in synchrotron radiation sources delivering intense brilliant X-rays have enabled access to this liquid–liquid interface. X-ray investigations of layering and charge effects provided new insight into the atomic structure specifically (Barton *et al.*, 1986; Bosio *et al.*, 1984; Dimasi *et al.*, 1998; Magnussen *et al.*, 1995; Duval *et al.*, 2012). Studies of interface charge transfer at immiscible liquid–liquid interfaces and nanoparticle growth (Gründer *et al.*, 2011) are key to understanding these processes and offer interesting applications, for example for the production of nanoparticles by electrodeposition (Carim *et al.*, 2011).

In a first atomic-resolution X-ray reflectivity study of liquid-mercury electrodes in a simple electrolyte solution (0.1 M NaF), the interfacial layering of the Hg atoms at the liquid Hg–electrolyte interface has been verified (Elsen *et al.*, 2010). By reproducing these experiments at LISA we have demonstrated the ability to record high-quality X-ray reflectivity curves at a liquid–liquid interface with LISA (Fig. 13). Additionally, due to the novel set-up of the diffractometer, which avoids the movement of the sample during the reflectivity, we were able to reduce the measurement time to 57 min which is about half that of the previous measurements.

By using a more complex electrolyte solution, adsorption of solution species at the liquid mercury electrode can be studied. Electrochemical methods can give quantitative information about the adsorbed surface excess but not directly on the structure of the adsorbed layer, whereas X-ray reflectivity can provide structural information up to the atomic scale. For this experiment the electrolyte was changed to a mixture of 0.01 M NaF, 0.01 M NaBr and 0.25 mM PbBr₂. X-ray reflectivity measurements have been carried out to reveal structural information perpendicular to the interface on an atomic scale. During the X-ray reflectivity measurements the interface was held under electrochemical control to create a defined electrochemically adsorbed layer on the mercury electrode and to be able to investigate a possible effect of the applied potential on the adsorbed layer. Our measurements show that we can reversibly adsorb a lead-containing layer at the Hg–electrolyte interface. At potentials negative of the adsorption peak at -0.7 V (relative to the Hg/Hg₂SO₄ reference electrode) in the cyclic voltammogram [Fig. 13(*a*), inset] the reflectivity reveals

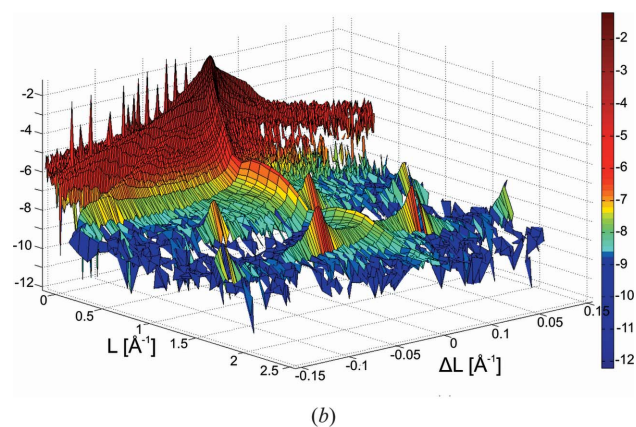
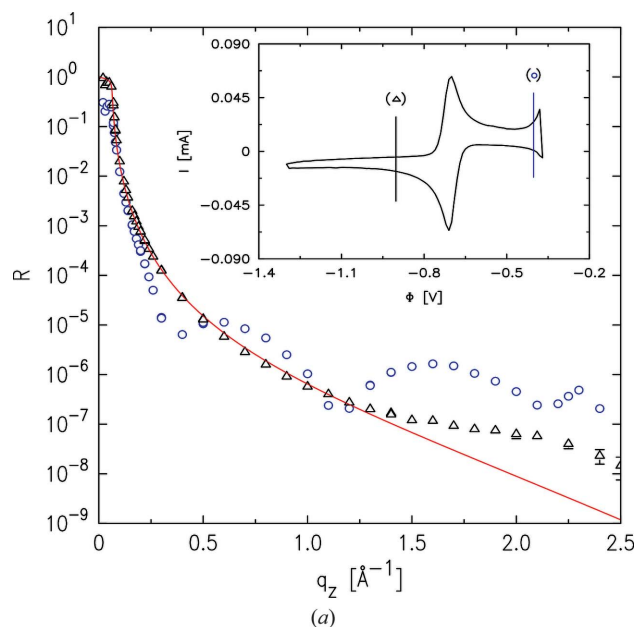


Figure 13 Structural investigation of the Hg–0.01 M NaF + 0.01 M NaBr + 0.25 mM PbBr₂ electrochemical interface: (*a*) X-ray reflectivity curves of the mercury–electrolyte interface at -0.75 V (black) and -0.28 V (blue). Inset: cyclic voltammogram of the investigated system (potentials of X-ray reflectivities marked). All potentials are given relative to the Hg/Hg₂SO₄ electrode. (*b*) Intensity map of the reflectivity with the one-dimensional Mythen detector located in the plane of the beam showing Bragg reflections of a crystalline component in addition to the monolayer observed in the specular reflectivity.

no significant differences compared with the Hg–0.01 M NaF interface, whereas at potentials positive of -0.7 V oscillations are found in the reflectivity, indicating the formation of an adsorbate layer with a thickness of 7–8 Å. In addition to the adsorbate layer, powder-like crystals were also observed (Fig. 13*b*). A detailed description of this complex electrochemical system is given elsewhere (Elsen *et al.*, 2013).

7.3. Reflectivity studies on lipid monolayers at the liquid–liquid interface

The interest in liquid–liquid emulsions is far reaching, ranging from simple cases such as found in food science and

cosmetics to the complex bio-membranes of living cells. Movement of a solute from one liquid phase to another plays a vital role in the chemical industry, for example in liquid–liquid extraction processes, and in many biological systems (Barnes & Gentle, 2005). The role of membrane barriers is significant in understanding these transport mechanisms and hence key to understanding many biological processes (Frielingsdorf *et al.*, 2008; Hou *et al.*, 2006; Klösgen *et al.*, 1989; Müller & Klösgen, 2005). Phospholipids are biological building blocks and understanding their structure and function in membranes under realistic conditions, *i.e.* at the liquid–liquid interface, is pivotal. Common methods of studying membrane structures, *i.e.* (i) electron microscopy (imaging and diffraction), atomic force microscopy (Klösgen *et al.*, 2002), (ii) nuclear magnetic resonance spectroscopy, (iii) diffraction studies of membrane stacks dry (Angelova *et al.*, 1997; Ivanova *et al.*, 1996) and at the liquid–solid interface (Gutberlet *et al.*, 2004*a,b*), and (iv) small-angle scattering of vesicles, have all contributed to understanding of the membrane structure (Barnes & Gentle, 2005). In contrast to these methods, scattering studies of a membrane at a single liquid–liquid interface would allow one to investigate the membranes in their native environment and to apply chemical and potential gradients. Additionally, one of the few X-ray reflectivity studies of surfactant monolayers (long-chain *n*-alkanoic and *n*-alkanol monolayers) at a liquid–liquid (water–perfluorohexane) interface (Tikhonov *et al.*, 2006) shows stark conformational changes as compared with those seen at the water–vapour interface, reinforcing the need for studies in the native liquid environment.

An understanding of the functionality of biological membranes requires not only the structural integration of the proteins, that are often assumed to provide the specific functions; the structural arrangement of the lipids, forming the matrix of a membrane, has to be known as well. Some aspects of a biological membrane in a natural-like environment can be modelled by a lipid monolayer at the water–oil interface (Schlossman *et al.*, 1999). With X-ray reflectivity the electron density profile of the lipid monolayer can be determined, thus giving the molecular structure of the layer normal to the interface on a submolecular scale. A lipid monolayer at the water–oil interface can be formed by the self-assembly of the lipids due to the hydrophilic and hydrophobic properties of the head and the chain group of the lipid molecule. In this study the lipid 1-palmitoyl-2-oleyl-*sn*-glycero-3-phosphocholine (POPC) formed a monolayer at the water–perfluorohexane interface. The formation of the lipid monolayer at the water–perfluorohexane interface was achieved by dissolving the lipid in the pure perfluorohexane and adding the water onto the perfluorohexane surface. We chose perfluorohexane as the second liquid phase as it provides a good contrast with water. In Fig. 14 an X-ray reflectivity curve from the weakly scattering POPC monolayer is shown. The modulation seen at 0.25 \AA^{-1} is evidence of the POPC in perfluorohexane with a combined head and tail length of $\sim 25 \text{ \AA}$ at the perfluorohexane–water interface (Elsen *et al.*, 2013). This is in agreement with expected values (Sun *et al.*, 1996). The roughness measured at the interface was estimated to be 8 \AA .

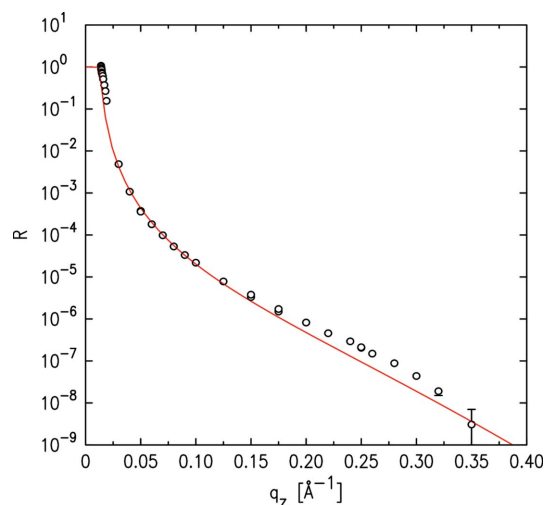


Figure 14

Reflectivity of a POPC monolayer at the C_6F_{14} –water interface (symbols) self-assembled from a saturated solution of the lipid in C_6F_{14} . The Fresnel reflectivity, convoluted by a surface roughness of 8 \AA , is shown for comparison (red line).

8. Conclusions

The Liquid Interfaces Scattering Apparatus (LISA) at the P08 beamline of the PETRA III synchrotron radiation source at DESY is a dedicated diffractometer for liquid surfaces and liquid–liquid interfaces. The use of an asymmetric tilting double-crystal monochromator in Bragg geometry allows studies without moving the sample as well as complete mechanical decoupling of the sample from the rest of the diffractometer, providing ultimate sample stability. The large accessible vertical and lateral wavevector transfers and the wide energy range of 6.4 to 29.4 keV opens up opportunities for addressing a plethora of problems in fundamental and applied liquid interface science.

We acknowledge funding for LISA by BMBF grants 05ks7fk3 and 05k10fk2 and for the UHV magnetic chamber by SFB855. We thank the staff at PETRA III and in particular our colleagues at the P08 beamline for their excellent support.

References

- Abes, M., Koops, C. T., Hrkac, S. B., Greve, H., Quandt, E., Collins, S. P., Murphy, B. M. & Magnussen, O. M. (2013). *Appl. Phys. Lett.* **102**, 011601.
- Als-Nielsen, J. (1984). *Physica B/C*, **126**, 145–148.
- Angelova, A., Ionov, R. & Gutberlet, T. (1997). *Thin Solid Films*, **305**, 309–315.
- Arnold, T., Nicklin, C., Rawle, J., Sutter, J., Bates, T., Nutter, B., McIntyre, G. & Burt, M. (2012). *J. Synchrotron Rad.* **19**, 408–416.
- Barnes, G. T. & Gentle, I. R. (2005). *Interface Science*, 1st ed. Oxford University Press.
- Barthelmess, M., English, U., Pflüger, J., Schöps, H., Skupin, J. & Tischer, M. (2008). *Proceedings of the 11th European Particle Accelerator Conference (EPAC08)*, Genoa, Italy, p. 2320.
- Barton, S. W., Thomas, B. N., Novak, F., Weber, P. M., Harris, J., Dolmer, P., Bloch, J. M. & Rice, S. A. (1986). *Nature (London)*, **321**, 685–687.
- Bosio, L., Cortes, R., Defrain, A. & Oumezine, M. (1984). *J. Non-Cryst. Solids*, **61–62**, 697–702.

- Braslau, A., Deutsch, M., Pershan, P. S., Weiss, A. H., Als-Nielsen, J. & Bohr, J. (1985). *Phys. Rev. Lett.* **54**, 114–117.
- Braslau, A., Pershan, P. S., Swislow, G., Ocko, B. M. & Als-Nielsen, J. (1988). *Phys. Rev. A*, **38**, 2457–2470.
- Buess-Herman, C. (1986). *Trends in Interfacial Electrochemistry*, edited by A. F. Silva, pp. 205–253. Dordrecht: Reidel.
- Carim, A. I., Collins, S. M., Foley, J. M. & Maldonado, S. (2011). *J. Am. Chem. Soc.* **133**, 13292–13295.
- Chaize, J. M., Götz, A., Klotz, W. D., Meyer, J., Perez, M., & Taurel, E. (1999). *International Conference on Accelerator and Large Experimental Physics Control Systems*, pp. 475–479.
- Chapman, D. L. (1913). *Philos. Mag.* **25**, 6.
- Dailant, J., Bosio, L., Benattar, J. J. & Meunier, J. (1989). *Europhys. Lett.* **8**, 453–458.
- Deutsch, M., Wu, X. Z., Sirota, E. B., Sinha, S. K., Ocko, B. M. & Magnussen, O. M. (1995). *Europhys. Lett.* **30**, 283–288.
- Dimasi, E., Tostmann, H., Ocko, B. M., Pershan, P. S. & Deutsch, M. (1998). *Phys. Rev. B*, **58**, R13-419–R13-422.
- Duval, J. F. L., Bera, S., Michot, L. J., Dailant, J., Belloni, L., Konovalov, O. & Pontoni, D. (2012). *Phys. Rev. Lett.* **108**, 206102.
- Elsen, A., Festeren, S., Runge, B., Kooops, C. T., Ocko, B. M., Deutsch, M., Seeck, O. H., Murphy, B. M. & Magnussen, O. M. (2013). *Proc. Natl Acad. Sci.* **110**, 6663–6668.
- Elsen, A., Murphy, B. M., Ocko, B. M., Tamam, L., Deutsch, M., Kuzmenko, I. & Magnussen, O. M. (2010). *Phys. Rev. Lett.* **104**, 105501.
- Frielingsdorf, S., Jakob, M. & Klösgen, R. B. (2008). *J. Biol. Chem.* **283**, 33838–33845.
- Fukuto, M., Heilmann, R. K., Pershan, P. S., Yu, S. J. M., Griffiths, J. A. & Tirrell, D. A. (1999). *J. Chem. Phys.* **111**, 9761–9777.
- Gouy, M. (1910). *J. Phys. Theor. Appl.* **9**, 457–468.
- Gründer, Y., Ho, H. L. T., Mosselmans, J. F. W., Schroeder, S. L. M. & Dryfe, R. A. W. (2011). *Phys. Chem. Chem. Phys.* **13**, 15681–15689.
- Gutberlet, T., Klosgen, B., Krastey, R. & Steitz, R. (2004a). *Adv. Eng. Mater.* **6**, 832–836.
- Gutberlet, T., Steitz, R., Fragneto, G. & Klosgen, B. (2004b). *J. Phys. Condens. Matter*, **16**, S2469–S2476.
- Helmholtz, H. (1879). *Ann. Phys.* **243**, 337–382.
- Honkimäki, V., Reichert, H., Okasinski, J. S. & Dosch, H. (2006). *J. Synchrotron Rad.* **13**, 426–431.
- Hou, B., Frielingsdorf, S. & Klösgen, R. B. (2006). *J. Mol. Biol.* **355**, 957–967.
- Ivanova, T. I., Frank-Kamenetskaya, O. V., Drits, V. A., Kastowsky, M., Gutberlet, T. & Bradaczek, H. (1996). *Thin Solid Films*, **279**, 228–232.
- Klösgen, R. B., Saedler, H. & Weil, J. H. (1989). *Mol. Gen. Genet.* **217**, 155–161.
- Klösgen, B., Spangenberg, T., Niehus, H., Gutberlet, T., Steitz, R. & Fragneto, G. (2002). *Cell. Mol. Biol. Lett.* **7**, 240.
- Kraack, H., Ocko, B. M., Pershan, P. S., Sloutskin, E. & Deutsch, M. (2002). *Science*, **298**, 1404–1407.
- Laanait, N., Mihaylov, M., Hou, B. Y., Yu, H., Vanýsek, P., Meron, M., Lin, B. H., Benjamin, I. & Schlossman, M. L. (2012). *Proc. Natl Acad. Sci. USA*, **109**, 20326–20331.
- Lin, B. H., Meron, M., Gebhardt, J., Graber, T., Schlossman, M. L. & Viccaro, P. J. (2003). *Physica B*, **336**, 75–80.
- Luo, G. M., Malkova, S., Yoon, J., Schultz, D. G., Lin, B. H., Meron, M., Benjamin, I., Vanýsek, P. & Schlossman, M. L. (2006). *Science*, **311**, 216–218.
- Magnussen, O. M., Ocko, B. M., Deutsch, M., Regan, M. J., Pershan, P. S., Abernathy, D., Grübel, G. & Legrand, J. F. (1996). *Nature (London)*, **384**, 250–252.
- Magnussen, O. M., Ocko, B. M., Regan, M. J., Penanen, K., Pershan, P. S. & Deutsch, M. (1995). *Phys. Rev. Lett.* **74**, 4444–4447.
- Müller, M. & Klösgen, R. B. (2005). *Mol. Membr. Biol.* **22**, 113–121.
- Murphy, B. M., Greve, M., Runge, B., Kooops, C. T., Elsen, A., Stettner, J., Seeck, O. H. & Magnussen, O. M. (2010). *AIP Conf. Proc.* **1234**, 155–158.
- Nave, C. & Garman, E. F. (2005). *J. Synchrotron Rad.* **12**, 257–260.
- Ocko, B. M., Wu, X. Z., Sirota, E. B., Sinha, S. K. & Deutsch, M. (1994). *Phys. Rev. Lett.* **72**, 242–245.
- Paithankar, K. S. & Garman, E. F. (2010). *Acta Cryst.* **D66**, 381–388.
- Pershan, P. S. & Als-Nielsen, J. (1984). *Phys. Rev. Lett.* **52**, 759–762.
- Pershan, P. S., Braslau, A., Weiss, A. H. & Als-Nielsen, J. (1987). *Phys. Rev. A*, **35**, 4800–4813.
- Pershan, P. S. & Schlossman, M. L. (2012). *Liquid Surfaces and Interfaces: Synchrotron X-ray Methods*. Cambridge University Press.
- Regan, M. J., Pershan, P. S., Magnussen, O. M., Ocko, B. M., Deutsch, M. & Berman, L. E. (1997). *Phys. Rev. B*, **55**, 15874–15884.
- Schlossman, M. L., Mitrinovic, D. M., Zhang, Z., Li, M. & Huang, Z. (1999). *Synchrotron Radiat. News*, **12**, 53–58.
- Schlossman, M. L., Synal, D., Guan, Y. M., Meron, M., Shearman, McCarthy, G., Huang, Z. Q., Acero, A., Williams, S. M., Rice, S. A. & Viccaro, P. J. (1997). *Rev. Sci. Instrum.* **68**, 4372.
- Schlossman, M. L. & Tikhonov, A. M. (2008). *Annu. Rev. Phys. Chem.* **59**, 153–177.
- Schwartz, D. K., Schlossman, M. L., Kawamoto, E. H., Kellogg, G. J., Pershan, P. S. & Ocko, B. M. (1990). *Phys. Rev. A*, **41**, 5687–5690.
- Seeck, O. H., Deiter, C., Pflaum, K., Bertam, F., Beerlink, A., Franz, H., Horbach, J., Schulte-Schrepping, H., Murphy, B. M., Greve, M. & Magnussen, O. (2012). *J. Synchrotron Rad.* **19**, 30–38.
- Shpyrko, O., Fukuto, M., Pershan, P., Ocko, B., Kuzmenko, I., Gog, T. & Deutsch, M. (2004). *Phys. Rev. B*, **69**, 245423.
- Shpyrko, O. G., Streitl, R., Balagurusamy, V. S. K., Grigoriev, A. Y., Deutsch, M., Ocko, B. M., Meron, M., Lin, B. & Pershan, P. S. (2006). *Science*, **313**, 77–80.
- Smilgies, D.-M., Boudet, N., Struth, B. & Konovalov, O. (2005). *J. Synchrotron Rad.* **12**, 329–339.
- Stepanov, S. (2013). *X-ray Server*, <http://sergey.gmca.aps.anl.gov/>.
- Sun, W. J., Tristram-Nagle, S., Suter, R. M. & Nagle, J. F. (1996). *Biophys. J.* **71**, 885–891.
- Swislow, G. (1996). *Spec. Certified Scientific Software*, Cambridge, MA, USA.
- Tamam, L., Pontoni, D., Sapir, Z., Yefet, S., Sloutskin, E., Ocko, B. M., Reichert, H. & Deutsch, M. (2011). *Proc. Natl Acad. Sci. USA*, **108**, 5522–5525.
- Tikhonov, A. M., Patel, H., Garde, S. & Schlossman, M. L. (2006). *J. Phys. Chem. B*, **110**, 19093–19096.
- Weinbach, S. P., Kjaer, K., Bouwman, W. G., Grübel, G., Legrand, J. F., Als-Nielsen, J., Lahav, M. & Leiserowitz, L. (1994). *Science*, **264**, 1566–1570.
- Weiss, A. H., Deutsch, M., Braslau, A., Ocko, B. M. & Pershan, P. S. (1986). *Rev. Sci. Instrum.* **57**, 2554.
- Wu, X. Z., Ocko, B. M., Sirota, E. B., Sinha, S. K., Deutsch, M., Cao, B. H. & Kim, M. W. (1993). *Science*, **261**, 1018–1021.
- Yano, Y. F., Uruga, T., Tanida, H., Toyokawa, H., Terada, Y., Takagaki, M. & Yamada, H. (2009). *Eur. Phys. J. Spec. Top.* **167**, 101–105.